ISIJ International, Vol. 50 (2010), No. 12, pp. 1859–1866

Prediction of Solidification Paths for Fe–C–Cr Alloys by a Multiphase Segregation Model Coupled to Thermodynamic Equilibrium Calculations

Hongwei ZHANG,[1,2] Charles-André GANDIN,[1] Haithem Ben HAMOUDA,[1,3] Damien TOURRET,[1] Keiji NAKAJIMA[4] and Jicheng HE[2]

1) MINES-ParisTech, CEMEF UMR CNRS 7635, BP 207, 06904 Sophia Antipolis, France.
2) Key Laboratory of Electromagnetic Processing of Materials, Ministry of Education, Northeastern University, Shenyang 110004 P.R. China. 3) Snecma-SAFRAN Group, BP48, 92234 Gennevilliers, France. 4) Department of Materials Science and Engineering, Royal Institute of Technology, SE-100 44 Stockholm, Sweden.

(*Received on May 20, 2010; accepted on August 23, 2010*)

A microsegregation model for the solidification of multicomponent alloys is developed. It couples the volume-averaged conservation equations for total mass, solute mass and energy assuming a uniform temperature. The diffusion in the liquid and solid phases, the growth kinetics of the solidifying microstructures and the velocity of the solid/liquid and solid/solid phase interfaces are considered in the model. Equilibrium between phases is taken into account and computed using dedicated thermodynamic software. The thermodynamic properties and their evolutions during solidification are directly retrieved from a database. Illustration is provided by the solidification of a Fe–C–Cr alloy. The occurrence of the recalescence due to the growth of the microstructure and the progress of solidification are predicted. The solidification behavior near to recalescence is evaluated. By adjusting the cooling intensity and the solute diffusivities, extreme approximations are retrieved. The model shows potentials to be coupled with a macrosegregation model for application to the solidification of multicomponent alloys.

KEY WORDS: solidification; microsegregation; multicomponent; dendritic structure; modeling.

1. Introduction

Most industrial applications in metal processing deal with multicomponent alloy systems. The segregation pattern during the solidification process mainly determines the structures and properties of the final products. For example, hot tearing is observed to take place at grain boundaries of the steel strained during solidification, together with preferred segregation at grain boundaries, *e.g.* segregation of trace elements such as P in steels.[1] Similarly, the size of the solidification grain structures and the intergranular fraction of secondary phases in aluminum alloys are known to have significant effects on the formation of hot cracks.[2] Better understanding of hot tearing in alloys requires distinguishing between intra and intergranular segregations, which is the field of on-going research.[3]

Wang and Beckermann[4] developed Rappaz and Thévoz segregation model[5] for equiaxed dendritic solidification to consider the back-diffusion in solid. Rappaz and Boettinger[6] and Appolaire *et al.*[7] applied the model to multicomponent alloys with the simplification of uniform composition in interdendritic liquid region and linearized phase diagrams. The latter assumption could be removed by Tourret and Gandin, the formulation of non-complete mixing of solute in the interdendritic liquid offering the possibility to deal with concurrent dendritic, peritectic and eutectic structures.[8] Some validations of the predictions could also be reached with measured fractions of the peritectic and eutectic microstructures in binary aluminum–nickel alloys,[8] as well as with the eutectic microstructure in binary aluminum–copper alloys,[9] considering several alloy compositions and cooling rates.

The present paper presents an extention of the microsegregation model developed by Tourret and Gandin to multicomponent alloy systems. One of the main interests of the model presented hereafter is its direct coupling with equilibrium calculations using a thermodynamic software and an appropriate database. For the sake of illustration, simulations are performed for primary dendritic solidification in the Fe–C–Cr system.[10] The predicted solidification paths are compared with those given by several approximations: full equilibrium or lever rule,[11,12] Gulliver–Scheil[13–16] and a mixed approximation known as partial equilibrium.[10,11]

2. Mathematical Model

2.1. Assumptions

The assumptions of the multicomponent microsegregation model are listed hereafter. **Figure 1** is provided for a clearer presentation. It is based on volume averaging tech-

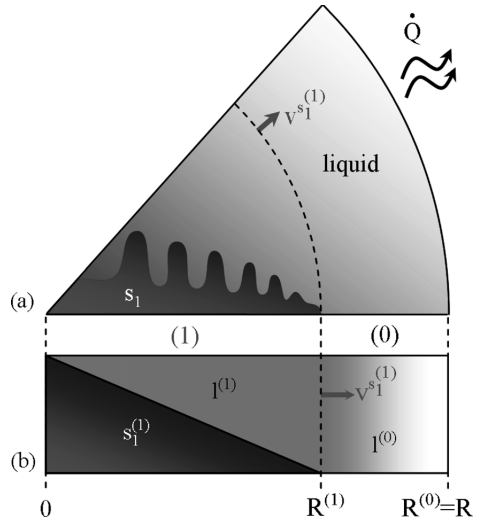

Fig. 1. Schematic distribution of the solid phase, s_1, and the liquid phase, l, in the extradendritic domain, (0), and the interdendritic domain, (1). Distinction is made between the solid phase, $s_1^{(1)}$, and the liquids of different compositions, $l^{(0)}$ and $l^{(1)}$. The dendritic microstructure nucleates at the center of a spherical geometry with radius R schematized in (a). The assumption of a radial propagation of the leading dendrite tips permits a one-dimensional spherical approximation. The boundary between mushy zone (1)=$s_1^{(1)}$+$l^{(1)}$ and extradendritic liquid (0)=$l^{(0)}$ is located at position $R^{(1)}$ shown in (b).

nique of the heat and mass exchanges considering a multiphase system with equal and constant densities, ρ, in all phases and fixed phases, $v^{\alpha}=0$.[4,8]

- The system chosen is a one-dimensional spherical domain of radius R with an external surface A and a volume V.
- Nucleation of the first solid phase, s_1, occurs at the center of the domain in an undercooled liquid, l.
- Upon radial growth, s_1 develops as a dendritic microstructure. Two zones can then be defined as a function of the position of the boundary between the dendrite tips and the undercooled liquid, labeled $R^{(1)}$ in Fig. 1. The inner spherical core defined by $R^{(1)}$ contains a mushy zone, *i.e.* a mixture of the s_1 solid phase in zone (1), $s_1^{(1)}$, and of the l liquid phase in zone (1), $l^{(1)}$. The outer zone contains a liquid in zone (0), $l^{(0)}$.
- Mass exchanges are considered at interfaces $s_1^{(1)}/l^{(1)}$ and $l^{(1)}/l^{(0)}$. This means that mass exchanges at the interface $s_1^{(1)}/l^{(0)}$ are neglected when building the microsegregation model.
- Due to the large value of the Lewis number for metallic alloys, the temperature is assumed uniform.
- Equilibrium at all phase interfaces is assumed.
- A dendrite tip kinetics for multicomponent alloy system can be used, which is based on the Ivantsov solution for the diffusion field outside a paraboloidal dendrite tip growing at a fixed velocity in a stagnant undercooled melt with a uniform composition[12]; the working point of the dendritie tip being assumed to follow the marginal stability approximation.[18]

Note that the last three approximations mean that the model is only valid for low supersaturations of the melt, when thermal undercooling and departure from interface equilibrium can be assumed.

2.2. Averaged Equations

With the assumptions listed above, and further neglecting the macroscopic diffusion fluxes, the following forms of the conservation equations can be written, respectively for the total mass and the solute mass of a phase α surrounding by α/β interfaces:

$$\frac{\partial g^{\alpha}}{\partial t}=\sum_{\beta\,(\beta\neq\alpha)} S^{\alpha/\beta}v^{\alpha/\beta} \quad \text{.....(1)}$$

$$g^{\alpha}\frac{\partial\langle w_i^{\alpha}\rangle^{\alpha}}{\partial t}=\sum_{\beta\,(\beta\neq\alpha)} S^{\alpha/\beta}(w_i^{\alpha/\beta}-\langle w_i^{\alpha}\rangle^{\alpha})\left(v^{\alpha/\beta}+\frac{D_i^{\alpha}}{l_i^{\alpha/\beta}}\right) \quad \text{.....(2)}$$

The corresponding interfacial balances between phase α and phase β can be written:

$$v^{\alpha/\beta}+v^{\beta/\alpha}=0 \quad \text{.....(3)}$$

$$(w_i^{\alpha/\beta}-w_i^{\beta/\alpha})v^{\alpha/\beta}+\frac{D_i^{\alpha}}{l_i^{\alpha/\beta}}(w_i^{\alpha/\beta}-\langle w_i^{\alpha}\rangle^{\alpha})+\frac{D_i^{\beta}}{l_i^{\beta/\alpha}}(w_i^{\beta/\alpha}-\langle w_i^{\beta}\rangle^{\beta})=0 \quad \text{....(4)}$$

where the following variables are defined in phase α: the volume fraction, g^{α}, the average composition of the solute element i, $\langle w_i^{\alpha}\rangle^{\alpha}$, the diffusion coefficient of solute element i, D_i^{α}. The other variables are defined at the α/β interface: the interfacial composition of solute element i, $w_i^{\alpha/\beta}$, the diffusion length for element i in phase α, $l_i^{\alpha/\beta}=-(w_i^{\alpha/\beta}-\langle w_i^{\alpha}\rangle^{\alpha})/(\partial w_i/\partial n)|_{\alpha/\beta}$, the normal evolution velocity, $v^{\alpha/\beta}$, the interfacial area concentration, $S^{\alpha/\beta}=A^{\alpha/\beta}/V$.

The additional uniform temperature approximation leads to the global energy balance:

$$\frac{\partial\langle H\rangle}{\partial t}=\sum_{\alpha}\left(\langle H^{\alpha}\rangle^{\alpha}\frac{\partial g^{\alpha}}{\partial t}+g^{\alpha}\frac{\partial\langle H^{\alpha}\rangle^{\alpha}}{\partial T}\frac{\partial T}{\partial t}+g^{\alpha}\sum_i\frac{\partial\langle H^{\alpha}\rangle^{\alpha}}{\partial\langle w_i^{\alpha}\rangle^{\alpha}}\frac{\partial\langle w_i^{\alpha}\rangle^{\alpha}}{\partial t}\right)=-\frac{h_{\mathrm{ext}}S_{\mathrm{ext}}}{\rho}(T-T_{\mathrm{ext}}) \quad \text{.....(5)}$$

where $\langle H\rangle$ is the averaged enthalpy of the system, $\langle H^{\alpha}\rangle^{\alpha}$ is the average enthalpy of phase α, ρ is the averaged density of the phases and T is the temperature of the system. The system exchanges heat with its surroundings kept at temperature T_{ext}. This is described by an apparent heat transfer coefficient, h_{ext}, that applies on the external area concentration, $S_{\mathrm{ext}}=A/V$.

2.3. Additional Relations

2.3.1. Dendrite Tip Growth Kinetics

The velocity of the boundary between zone (1) and zone (0), $v^{(1)/(0)}$, is set equal to the velocity of the dendrite tips of the $s_1^{(1)}$ solid phase growing into the $l^{(0)}$ liquid, $v^{s_1^{(1)}/l^{(0)}}$. Based on the model proposed by Rappaz and Boettinger, the undercooling at a dendrite tip for a multicomponent system is the summation of the constitutional undercooling over each

solute element i plus the curvature undercooling[6]:

$$T_{\mathrm{L}}(\langle w_i^{l^{(0)}}\rangle^{l^{(0)}}) - T = \sum_i \frac{\partial T}{\partial w_i^{l^{(0)}/s_1^{(1)}}} (\langle w_i^{l^{(0)}}\rangle^{l^{(0)}} - w_i^{l^{(0)}/s_1^{(1)}}) + \frac{2\Gamma}{r} \quad \text{.....(6)}$$

where $T_{\mathrm{L}}(\langle w_i^{l^{(0)}}\rangle^{l^{(0)}})$ is the temperature read on the liquidus surface of the multicomponent phase diagram at composition $\langle w_i^{l^{(0)}}\rangle^{l^{(0)}}$, $\partial T/\partial w_i^{l^{(0)}/s_1^{(1)}}$ is the slope of the liquidus surface with respect to the solute element i, Γ is the Gibbs–Thomson coefficient and r is dendrite tip radius. The liquid and solid compositions of the solute element i at the dendrite tip, respectively $w_i^{l^{(0)}/s_1^{(1)}}$ and $w_i^{s_1^{(1)}/l^{(0)}}$, are given through the definition of the supersaturation, Ω_i, and applying the assumption of thermodynamic equilibrium at the phase interface by introducing the segregation coefficient $k_i^{s_1^{(1)}/l^{(0)}}$:

$$\Omega_i = \frac{w_i^{l^{(0)}/s_1^{(1)}} - \langle w_i^{l^{(0)}}\rangle^{l^{(0)}}}{w_i^{l^{(0)}/s_1^{(1)}} - w_i^{s_1^{(1)}/l^{(0)}}} \quad \text{.....(7)}$$

$$k_i^{s_1^{(1)}/l^{(0)}} = \frac{w_i^{s_1^{(1)}/l^{(0)}}}{w_i^{l^{(0)}/s_1^{(1)}}} \quad \text{.....(8)}$$

The solution for the diffusion field outside a paraboloidal dendrite tip growing at a fixed velocity in a stagnant undercooled melt with a uniform composition is given by the Ivantsov function, Iv, of the chemical Peclet number for solute element i, Pe_i:

$$\Omega_i = \mathrm{Iv}(\mathrm{Pe}_i) = \mathrm{Pe}_i \exp(\mathrm{Pe}_i) E_1(\mathrm{Pe}_i) \quad \text{.....(9)}$$

$$\mathrm{Pe}_i = \frac{r v^{s_1^{(1)}/l^{(0)}}}{2D_i^l} \quad \text{.....(10)}$$

where $E_1(\mathrm{Pe}_i)$ is the first exponential integral.[12] All solute elements have to satisfy Eq. (10) for a given set of the tip radius, r, and the velocity, $v^{s_1^{(1)}/l^{(0)}}$. Thus, one can express the Peclet number of each solute element i, Pe_i, as a function of a unique Peclet number for a selected unique solute element j, Pe_j ($j \neq i$). Substitution of Eqs. (7)–(10) into Eq. (6) leads to an equation to solve for the unique unknown Pe_j.[17]

The marginal stability criterion writes[18]:

$$r^2 v^{s_1^{(1)}/l^{(0)}} = \frac{1}{4\pi^2} \sum_i \frac{D_i^l \Gamma}{(\partial T/\partial w_i^{l^{(0)}/s_1^{(1)}}) w_i^{l^{(0)}/s_1^{(1)}} (k_i^{s_1^{(1)}/l^{(0)}} - 1)} \quad \text{...(11)}$$

Combining Eqs. (10) and (11), the tip radius, r, is updated and an iterative procedure finally provides with the converged r and $v^{s_1^{(1)}/l^{(0)}}$.

2.3.2. Interfacial Area Concentrations and Diffusion Lengths

The interfacial area concentrations are evaluated as a function of the radial position of the mushy zone, $S^{l^{(1)}/l^{(0)}} = 3R^{(1)^2}/R^3$, and as a function of the dendrite arm spacing, λ_2, and the volume fraction of the mushy zone, $g^{(1)}$, $S^{l^{(1)}/s_1^{(1)}} = 2g^{(1)}/\lambda_2$, the latter expression assuming a plate-like geometry. The diffusion length in the solid phase from the $s_1^{(1)}/l^{(1)}$ interface is derived considering a parabolic composition profile: $l_i^{s_1^{(1)}/l^{(1)}} = (g^{s_1^{(1)}}/g^{(1)})(\lambda_2/6)$. Similar assumptions for the interdendritic liquid phase from the $s_1^{(1)}/l^{(1)}$ interface leads to $l_i^{l^{(1)}/s_1^{(1)}} = (g^{l^{(1)}}/g^{(1)})(\lambda_2/6)$. The lengths $l_i^{s_1^{(1)}/l^{(1)}}$ and $l_i^{l^{(1)}/s_1^{(1)}}$ characterize diffusion at the scale of the dendritic microstructure localized in zone (1). Diffusion in the radial direction within the liquids $l^{(0)}$ and $l^{(1)}$ are also considered due to the presence of composition variations in the liquid. The mathematical expression for $l_i^{l^{(0)}/l^{(1)}}$ is made available elsewhere.[8] The simple choice of $l_i^{l^{(1)}/l^{(0)}} = l_i^{l^{(0)}/l^{(1)}}$ is made to also account for the diffusion in the interdendritic liquid $l^{(1)}$.

2.3.3. Compositions and Velocity at Interface $s_1^{(1)}/l^{(1)}$

The assumption of phase interface equilibrium leads to the two following relationships:

$$T_{\mathrm{L}}(\langle w_i^{l^{(1)}}\rangle^{l^{(1)}}) - T = \sum_i \frac{\partial T}{\partial w_i^{l^{(1)}/s_1^{(1)}}} (\langle w_i^{l^{(1)}}\rangle^{l^{(1)}} - w_i^{l^{(1)}/s_1^{(1)}}) \quad \text{....(12)}$$

$$k_i^{s^{(1)}/l^{(1)}} = \frac{w_i^{s_1^{(1)}/l^{(1)}}}{w_i^{l^{(1)}/s_1^{(1)}}} \quad \text{.....(13)}$$

Equations (4), (12), and (13) provide a complete system since the temperature, T, and velocity, $v^{s_1^{(1)}/l^{(1)}}$, must be uniquely defined. A solution is provided by the substitution of Eq. (13) into Eq. (4) to replace the solid compositions $w_i^{s_1^{(1)}/l^{(1)}}$, further using the unique velocity $v^{s_1^{(1)}/l^{(1)}}$ for all species in Eq. (4) to obtain the expressions of $w_i^{l^{(1)}/s_1^{(1)}}$ as a function of a unique chemical species $w_j^{l^{(1)}/s_1^{(1)}}$ ($j \neq i$), then substituting the latter relations $w_i^{l^{(1)}/s_1^{(1)}}$ ($w_j^{l^{(1)}/s_1^{(1)}}$) into Eq. (12). Knowing the thermodynamic properties $k_i^{s_1^{(1)}/l^{(1)}}$ and $\partial T/\partial w_i^{l^{(1)}/s_1^{(1)}}$ for each solute species i, Eq. (12) can then be solved to find $w_j^{l^{(1)}/s_1^{(1)}}$ and, consecutively, all phase interface compositions and the velocity.

2.3.4. Compositions at Boundary $l^{(0)}/l^{(1)}$

A continuity condition for the compositions at the $l^{(0)}/l^{(1)}$ boundary is used, *i.e.* $w_i^{l^{(0)}/l^{(1)}} = w_i^{l^{(1)}/l^{(0)}}$. Applying Eq. (4) for this boundary simply leads to:

$$w_i^{l^{(1)}/l^{(0)}} = \left(\frac{D_i^l}{l_i^{l^{(0)}/l^{(1)}}} \langle w_i^{l^{(0)}}\rangle^{l^{(0)}} + \frac{D_i^l}{l_i^{l^{(1)}/l^{(0)}}} \langle w_i^{l^{(1)}}\rangle^{l^{(1)}} \right) \Bigg/ \left(\frac{D_i^l}{l_i^{l^{(0)}/l^{(1)}}} + \frac{D_i^l}{l_i^{l^{(1)}/l^{(0)}}} \right) \quad \text{.....(14)}$$

2.3.5. Thermodynamic Data and Phase Equilibrium

By directly coupling with the Thermo-Calc software using the PTERN database[19] for the Fe–C–Cr system, the following thermodynamic data and phase equilibrium parameters can be directly accessed:

- $\langle H^\alpha\rangle^\alpha$, the average enthalpy of phase α at the average composition $\langle w_i^\alpha\rangle^\alpha$ and temperature T,
- $\partial\langle H^\alpha\rangle^\alpha/\partial T$, the temperature derivative of the average enthalpy of phase α at the average composition $\langle w_i^\alpha\rangle^\alpha$ (also known as heat capacity),
- $\partial\langle H^\alpha\rangle^\alpha/\partial\langle w_i^\alpha\rangle^\alpha$, the composition derivative of the average enthalpy of phase α at temperature T,
- $k_i^{s_1^{(1)}/l^{(0)}}$ and $k_i^{s_1^{(1)}/l^{(1)}}$, the partition ratio for the chemical solute element i between the solid and liquid phases, respectively at interface compositions $w_i^{l^{(0)}/s_1^{(1)}}$ and $w_i^{l^{(1)}/s_1^{(1)}}$,
- $\partial T/\partial w_i^{l^{(0)}/s_1^{(1)}}$ and $\partial T/\partial w_i^{l^{(1)}/s_1^{(1)}}$, the slope of the liquidus surface for the chemical solute element i, respectively at the interface compositions $w_i^{l^{(0)}/s_1^{(1)}}$ and $w_i^{l^{(1)}/s_1^{(1)}}$.

3. Algorithm

Knowing the nominal composition of the alloy, the equilibrium liquidus temperature is determined by a thermodynamic equilibrium calculation. During cooling of the system, nucleation occurs when the undercooling is greater than the nucleation undercooling prescribed. The primary solid phase is then created at the centre of the spherical domain. The zone boundary velocity (Sec. 2.3.1), the interfacial area concentrations and the diffusion lengths (Sec. 2.3.2), the solid/interdendritic liquid interface compositions and velocity (Sec. 2.3.3), and the zone boundary compositions (Sec. 2.3.4) are first determined. These quantities are needed to solve the total mass conservation (Eq. (1)), the solute mass conservation (Eq. (2)) and the global energy balance (Eq. (5)) separately until convergence is reached. An implicit iterative scheme, the Gear method, is used to solve the equations. The outputs are the phase fractions, the average compositions of the phases and the system temperature.

4. Results and Discussions

4.1. Overall Solidification Paths for Fe–1wt%C–10wt%Cr Alloy

All properties required for the simulation are listed in **Table 1**. Note that the name of the database is given with an adequate reference. It is indeed part of the simulation data since it provides with all information required for equilibrium calculations and phase properties. Temperature and composition dependences of the phase density and the diffusion coefficients can also be retrieved from the thermodynamic databases. However, the present model does not yet account for these data. This explains the presence of a constant value for the density and the diffusion coefficients. All the simulations below also assume the presence of a constant pressure and a closed system.

Figure 2 presents the computed time evolution of the temperature for a Fe–1wt%C–10wt%Cr alloy. The liquidus temperature of the alloy is equal to 1 713.15 K. It is chosen as the initial temperature of the system. Since the nucleation undercooling is set to zero, nucleation proceeds immediately with $s_1^{(1)}$=FCC as the primary solidification phase. However, the supersaturation being small, the fraction of solid does not immediately increase. The system first cools down with a cooling rate of about 12 K s^{-1} from 0 to 0.5 s. This is clearly seen in Fig. 2 where the fraction of the mushy zone, $g^{(1)}$, and the fraction of the solid phase, $g^{s_1^{(1)}}$, are displayed. The cooling rate departs from its initial value only when these fractions start to increase, *i.e.* after 0.5 s. The second usual behavior expected and indeed observed is the recalescence. It takes place when the development of the mushy zone permits to release sufficient heat compared to that extracted from the outer surface of the system. The maximum of the recalescence is observed at around 1.5 s. At this time, the slope of curve $g^{(1)}(t)$ does indeed decrease, its maximum being reached at the beginning of the recalescence. Note that the fraction of solid at the end of the recalescence is less than 0.05. All these behaviors are well known and described into details in the literature.[4–9)]

Several solidification paths are shown in **Fig. 3** considering the variation of the fraction of solid as a function of the temperature. The curve labeled P corresponds to the simulation result using the present microsegregation model. As

Table 1. Material parameters and initial and boundary conditions.

Thermodynamic database	PTERN			[19]
Density of the phases, ρ	7600			kg m^{-3}
Diffusion coefficients in liquid, D_i^l	i = C	10^{-8}	i = Cr 10^{-9}	m^2 s^{-1}
Diffusion coefficients in solid, D_i^s	i = C	10^{-9}	i = Cr 10^{-13}	m^2 s^{-1}
Nominal mass composition, $w_{i,0}$	i = C	1	i = Cr 10	wt %
Secondary dendrite arm spacing, λ_2	10^{-4}			m
Gibbs-Thomson parameter, Γ	$1.9 \cdot 10^{-8}$			K m
Radius of the system, R	10^{-3}			m
Initial temperature	1713.15			K
Nucleation undercooling	0			K
Heat transfer coefficient, h_{ext}	10			W m^{-2} K^{-1}
Surrounding temperature, T_{ext}	293			K

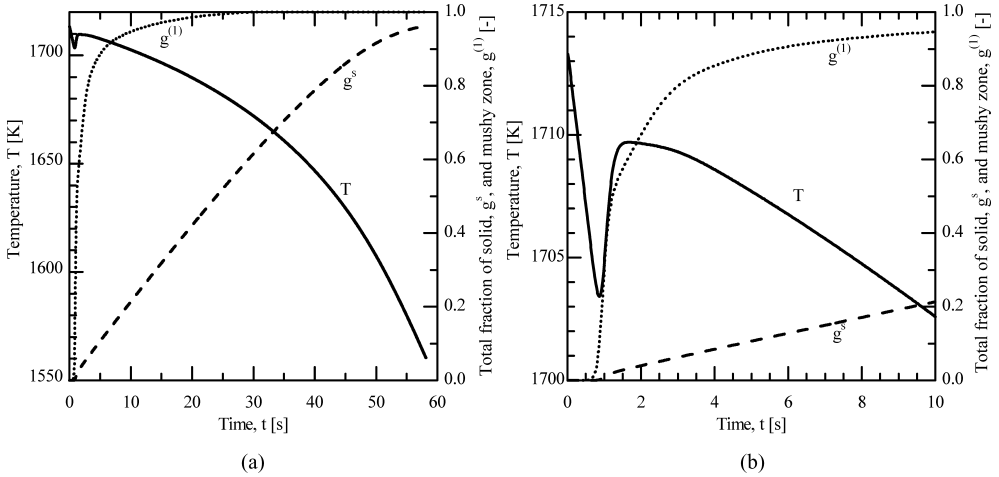

Fig. 2. Time evolutions of the temperature, T (plain line), the total fraction of solid, g^s (dashed line), and the fraction of the primary mushy zone, $g^{(1)}$ (dotted line), upon solidification of a Fe–1wt%C–10wt%Cr alloy.

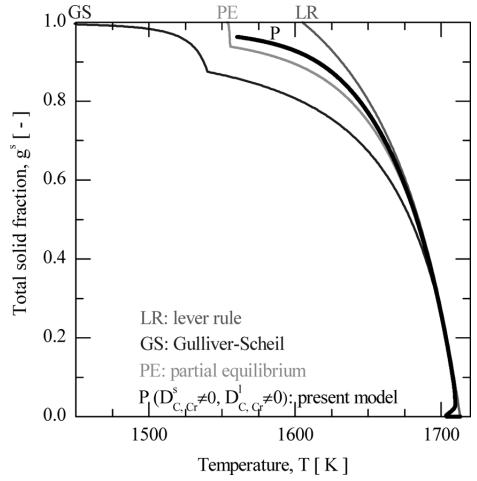

Fig. 3. Predicted total fraction of solid, g^s, *versus* temperature, T, for a Fe–1wt%C–10wt%Cr alloy using several approximations of the solidification path.

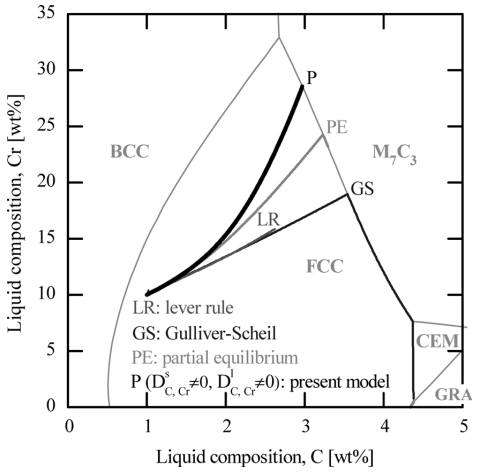

Fig. 4. Predicted liquid composition of Cr with respect to the liquid composition of C for a Fe–1wt%C–10wt%Cr alloy using various approximations of the solidification path. The thin grey curves delimit the domains of the liquidus surfaces for the various phases of the system. For the simulation using the present model, the average interdendritic liquid composition has been used, $\langle w^{l(1)}\rangle^{l(1)}=\langle w^{l(1)}_{Cr}\rangle^{l(1)}$ ($\langle w^{l(1)}_{C}\rangle^{l(1)}$).

can be seen, the fraction of solid first increases while the temperature also increases. This is due to the development of the solid phase upon recalescence shown in Fig. 2. The maximum of the temperature in Fig. 3 also corresponds to the end of the recalescence and solidification then continues to proceed while the temperature decreases. The curve abruptly stops at temperature 1 560 K while the fraction of solid has reached 0.96. At this temperature, other solid phases may form in the liquid and the present multicomponent model should be extended to account for concurrent solidification of several phases as was recently done for a binary alloy.[8] This observation is better seen with the solidification path drawn in **Fig. 4**, *i.e.* the evolution of the interdendritic liquid composition of Cr as a function of the interdendritic liquid composition of C. The thin grey curves delimit the domains of the liquidus surfaces for the various phases of the system. Starting from the nominal composition, the solidification path labeled P stops when reaching a eutectic valley that describes equilibrium between the liquid phase, the FCC phase and the M_7C_3 phase.

Comparison is useful to conduct by drawing the solidification paths for various assumptions. The curves labeled LR correspond to full thermodynamic equilibrium, meaning that all the phases have a uniform composition and are in equilibrium. As shown in Fig. 3, such a simulation leads to the full transformation of the liquid into the FCC primary phase at 1 605 K. This is also shown in Fig. 4 where the curve labeled LR stops on the liquidus surface of the FCC phase. This assumption of complete mixing of the chemical species through all the phases permits to write the simple solute mass balances and to retrieve the well known lever rule approximation.[11,12] It is yet not valid for metallic alloys because well mixed in phases requires very large values of the Fourier numbers for all chemical species, which is rarely satisfied in solidification processing. Another way to justify the limitation of the full equilibrium approximation is the fact that it does not predict the interdendritic phases that are yet most often observed. The Gulliver–Scheil approximation, labeled GS in Fig. 3, is thus generally preferred. It assumes no diffusion in the solid phases while the liquid phase is kept in a state of complete mixing. This difference is well justified when considering the ratio of the diffusivities in the liquid and solid phases that can easily reach several order of magnitude (see Table 1 for the orders of magnitude). With this approximation, thermodynamic equilibrium is verified only at the solid/liquid interface. The average solid composition does not follow equilibrium since no diffusion is permitted and the solid is made of an accumulation of the layers with varying compositions. One of the consequences is the delay of the solidification to lower temperatures, reaching the first eutectic valley with the fraction of the primary dendritic FCC phase of 0.87 at 1 540 K. The amount of liquid left being large, more eutectic structures can form. In the present simulation, the first eutectic structures take the form of the phases made of FCC, M_7C_3 and CEM(ENTITE) labeled in Fig. 4, the liquid composition following the various valleys defined by the intersection of the liquidus surfaces. Analysis of the mathematical formulation of this approximation also shows that final solidification can only be reached when the variance of the system is zero. For the present ternary alloy, this corresponds to a ternary eutectic (FCC+CEMENTITE+GRAPHITE) in equilibrium with the liquid phase taking place for a unique set of the phase composition and at a sensibly lower temperature. Finally, the last approximation is an intermediate solution considering full equilibrium in all phases only for C. It is therefore referred to as partial equilibrium and labeled PE in Figs. 3 and 4. With complete mixing in the liquid is considered for all elements as for the LR and GS cases, and similarly complete mixing is considered in the solid phases for C, no diffusion is assumed in the solid phases for Cr. These approximations are justified if C is an interstitial element and Cr is a substitutional element in the FCC phase. It is obvious from Figs. 3 and 4 that the PE equilibrium comes closer to the simulation using the presently developed microsegregation model (curves labeled P) accounting for diffusion. This is due to the large difference between the value of the diffusion coefficients used for C and Cr in the FCC phase, as can be read in Table 1.

4.2. Solidification Behavior Near Recalescence

Apart from the effect of diffusion in the FCC solid phase, the present multicomponent microsegregation model also considers diffusion in the liquid phase. We shall now analyze its effect in some details. **Figure 5** shows the time evolution of the average liquid compositions for the interdendritic liquid, the extradendritic liquid, and liquid composition at the interface between the solid and the two liquids, for both Cr and C. Considering the Fourier numbers in the solid and liquid phases, analyses of these curves can be done by ruling out the effect of the diffusion in the solid phase yet accounted for. Also one should note that the value chosen for diffusion of C in the liquid phase is 10 times greater than that for Cr. Finally, one should notice that the time scale is the same in Fig. 5 and in the right hand side part of Fig. 2.

The curves presenting the composition of the extradendritic liquid in contact with the solid phase is nothing but the liquid composition at the dendrite tip. As we discussed with Fig. 2, the growth velocity of the mushy zone/extradendritic liquid boundary reaches a maximum close to the minimum temperature prior to recalescence, *i.e.* at around 1 s. We can also see in Fig. 5 that the interface compositions $w_C^{l^{(0)}/s_1^{(1)}}$ and $w_{Cr}^{l^{(0)}/s_1^{(1)}}$ first increase rapidly and reach a maximum value at around 1 s. Besides, according to Eq. (7), the dendrite tip velocity is proportional to the supersaturation of the dendrite tip, *i.e.* to the difference between the liquid tip composition $w_i^{l^{(0)}/s_1^{(1)}}$ and the average extradendritic liquid composition $\langle w_i^{l^{(0)}} \rangle^{l^{(0)}}$. These differences are directly accessible for both i=Cr and i=C in Figs. 5(a) and 5(b), respectively. As we can see, the behavior for C is simpler compared to Cr. After reaching its maximum at the same time the recalescence begins, the increase of the temperature decreases the tip composition. The supersaturation of C consequently decreases. The tip composition then increases again at about 1.5 s. The accumulation of C in the extradendritic liquid due to mass exchange with the interdendritic liquid is sufficient to reduce the supersaturation. This time also corresponds to the maximum temperature after recalescence. It is of interest to report this evolution in the representation of Fig. 3. This is provided as interrupted lines in **Fig. 6**, superimposed onto the evolutions of the average interdendritic liquid with the same colors as shown in Fig. 4. There is no sign for recalescence on the composition curves predicted by LR, GS and PE approximations since neither the nucleation nor the evolution of the mushy zone is considered and a complete mixing in liquid is assumed during the thermodynamic equilibrium calculations. As shown in Fig. 6, at the beginning of solidification, these three colored curves don't show much difference. Among interrupted lines, the start of the recalescence corresponds to the position labeled *s*. The minimum of tip composition $w^{l^{(0)}/s_1^{(1)}}$ in carbon is labeled *e*_C, and corresponds as well to the end of the recalescence on the cooling curve, Fig. 2. At 1.5 s, the extradendritic liquid composition of Cr has not yet started to increase. It really starts to feel the accumulation of Cr due to the diffusion flux of solute leaving the mushy zone envelope at around 3.5 s, when the minimum tip composition of Cr is reached. This is also accessible in Figure 6 at position labeled *e*_Cr. Thus, the mushy zone dynamic and its effect on the cooling curve are found to mainly depend on the faster diffusing element, C, that is, the initial maximum on the tip composition curve (both for Cr and C

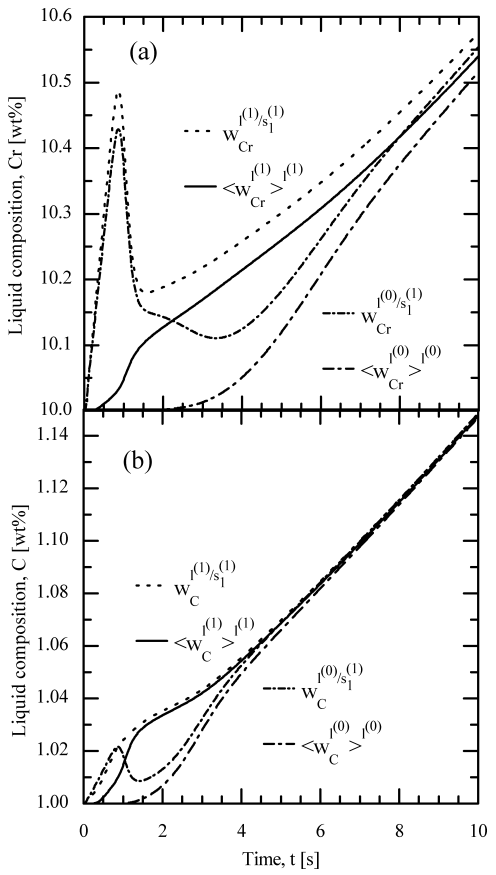

Fig. 5. Time evolutions of the average composition for the interdendritic liquid, $\langle w_i^{l^{(1)}} \rangle^{l^{(1)}}$, and the extradendritic liquid, $\langle w_i^{l^{(0)}} \rangle^{l^{(0)}}$, and the interfacial composition for the extradendritic liquid at the interface with the dendrite tip, $w_i^{l^{(0)}/s_1^{(1)}}$, and the interdendritic liquid at the interface with the primary dendritic solid phase, $w_i^{l^{(1)}/s_1^{(1)}}$, for (a) i=Cr and (b) i=C.

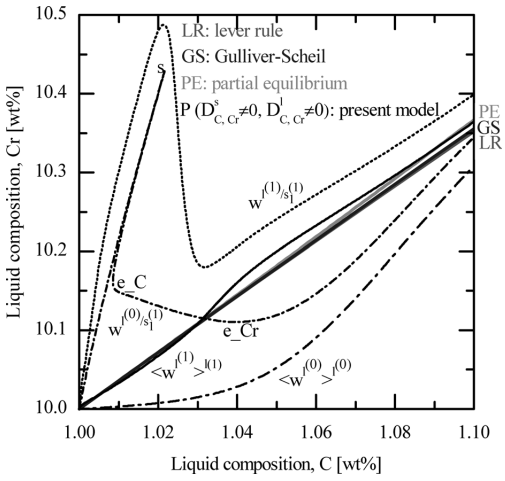

Fig. 6. Same as Fig. 4 (plain lines) in a narrow window with its minimum positioned at the alloy composition. Additional information is the average composition of the extradendritic liquid, $\langle w^{l^{(0)}} \rangle^{l^{(0)}} = \langle w_{Cr}^{l^{(0)}} \rangle^{l^{(0)}}$ ($\langle w_C^{l^{(0)}} \rangle^{l^{(0)}}$), the interfacial composition of the extradendritic liquid at the interface with the dendrite tip, $w^{l^{(0)}/s_1^{(1)}} = w_{Cr}^{l^{(0)}/s_1^{(1)}}$ ($w_C^{l^{(0)}/s_1^{(1)}}$), and the interdendritic liquid at the interface with the primary dendritic solid phase, $w^{l^{(1)}/s_1^{(1)}} = w_{Cr}^{l^{(1)}/s_1^{(1)}}$ ($w_C^{l^{(1)}/s_1^{(1)}}$).

in Figs. 5 and 6) corresponds to the minimum temperature before recalescence on the cooling curve (Fig. 2(b)) and the minimum on the tip composition curve of C is just related to the top of recalescence on the cooling curve. While the post-recalescence is mainly influenced by the slower diffusing element, Cr, and the solidification of the mushy zone, that is, after the minimum on the tip composition curve of Cr, the temperature begins to decrease sharply. The duration between the minimum of C and Cr on tip composition curves (Figs. 5 and 6) corresponds to the transition part after recalescence on cooling curve (Fig. 2(b)).

The behaviors commented above present similarities with those described by Rappaz and Boettinger.[6] However, several differences exist in the present model construction that permits to consider diffusion in the solid phase, non homogeneous interdendritic liquids, as well as direct coupling with thermodynamic calculations.

5. Conclusions

A multicomponent microsegregation model based on volume averaging has been developed considering the diffusion of each element in all phases and coupled with thermodynamic equilibrium calculations using Thermo-Calc. The model retrieves simple results such as the Gulliver–Scheil approximation when considering no diffusion in all solid phases. Considering the approximations given by full thermodynamic equilibrium (LR), no diffusion in solid (GS) and partial equilibrium (PE, *i.e.* LR for interstitial elements such as C and GS for substitutional elements such as Cr), the predicted solidification path by the present model is closer to PE due to the difference of liquid diffusivities used for C and Cr.

The recalescence and post-recalescence periods due to the growth of the mushy zone into the undercooled liquid are predicted. Interpretation involves finite diffusion in the liquid. It is explained based on the evolutions of the average composition in the extradendritic and interdendritic liquids as well as the interface compositions between these two liquids and the solid phase.

The implementation of the present multicomponent microsegregation model in a multiscale model for the prediction of grain structures is required if one wishes to access to a distinct description of intra and intergranular segregations of the nature and amount of the phase fractions in the as-cast state.[20] The model could also benefits from its extension to include the description of several solid phases (*i.e.* peritectic and eutectic microstructures as already available for binary alloys[8]).

Acknowledgments

This work was supported by Snecma-SAFRAN Group (France), 111 Project (No. B07015), Natural Science Foundation of Liaoning Province (No. 20031010 and No. 20072033) and the Fundamental Research Funds for the Central Universities (N100409004) (China).

Nomenclature

A: External surface area of a one-dimensional spherical domain
$A^{\alpha/\beta}$: Interfacial area at the interface α/β
D^{α}: Diffusion coefficient in phase α
g^{α}: Volume fraction of phase α
$g^{(a)}$: volume fraction of zone (a)
h_{ext}: Apparent heat transfer coefficient
$\langle H\rangle$: Averaged enthalpy of the system
$\langle H^{\alpha}\rangle^{\alpha}$: Average enthalpy of phase α
$\partial\langle H^{\alpha}\rangle^{\alpha}/\partial T$: Temperature derivative of the average enthalpy of phase α (*i.e.* heat capacity)
$\partial\langle H^{\alpha}\rangle^{\alpha}/\partial\langle w_i^{\alpha}\rangle^{\alpha}$: Composition derivative of the average enthalpy of phase α
$k^{\alpha/\beta}$: Segregation coefficient, (as defined by Eqs. (8), (13))
l: Liquid phase or diffusion length
$l^{\alpha/\beta}$: Diffusion length in phase α at the interface α/β
Pe: Peclet number, (as defined by Eq. (10))
r: Dendrite tip radius
R: Radius of a one-dimensional spherical domain
$R^{(a)}$: Radius of zone (a)
s_1: Primary solid phase
S_{ext}: External area concentration, $=A/V$
$S^{\alpha/\beta}$: Interfacial area concentration at the interface α/β, $=A^{\alpha/\beta}/V$
T: Temperature of the system
T_{ext}: Temperature of the surroundings
T_L: Liquidus surface temperature
$\partial T/\partial w^{l/\alpha}$: Slope of the liquidus surface with respect to the interface composition $w^{l/\alpha}$ (l, liquid; α, other phase)
v^{α}: Macroscopic flow velocity of phase α
$v^{(a)/(b)}$: Normal component of velocity at the boundary between zone (a) and zone (b)
$v^{\alpha/\beta}$: Normal component of the interface velocity for α solid phase at α/β interface
V: Volume of a one-dimensional spherical domain
$\langle w^{\alpha}\rangle^{\alpha}$: Average composition in phase α,
$w^{\alpha/\beta}$: Mass composition at the interface α/β

Greek

α: Phase
β: Phase
λ_2: Secondary dendrite arm spacing
ρ: Phase density
Γ: Gibbs–Thomson coefficient
Ω: Supersaturation, (as defined by Eq. (7))

Superscripts

(1): Interdendritic domain, *i.e.* zone (1)
(0): Extradendritic domain, *i.e.* zone (0)
(a)/(b): Boundary between zone (a) and zone (b)
l: Liquid
α: Phase
β: Phase
α/β: Interface between phase α and phase β

Subscripts

i: Solute element

REFERENCES

1) W. Kurz: *La Metallurgia Italiana*, (2008), 56.
2) D. G. Eskin, Suyitno and L. Katgerman: *Prog. Mater. Sci.*, **49** (2004), 629.
3) Ch.-A. Gandin: *Comptes Rendus Physique*, **11** (2010), 216.
4) C. Y. Wang and C. Beckermann: *Metall. Trans.*, **24A** (1993), 2787.
5) M. Rappaz and Ph. Thévoz: *Acta Mater.*, **35** (1987), 2929.

6) M. Rappaz and W. J. Boettinger: *Acta Mater.*, **47** (1999), 3205.
7) B. Appolaire, H. Combeau and G. Lesoult: *Mater. Sci. Eng.*, **487A** (2008), 33.
8) D. Tourret and Ch.-A. Gandin: *Acta Mater.*, **57** (2009), 2066.
9) Ch.-A. Gandin, S. Mosbah, Th. Volkmann and D. M. Herlach: *Acta Mater.*, **56** (2008), 3023.
10) Q. Chen and B. Sundman: *Mater. Trans.*, **43** (2002), 551.
11) M. Hillert: Phase Equilibria, Phase Diagrams and Phase Transformations, Cambridge University Press, Cambridge, UK, (1998), 155, 302.
12) J. A. Dantzig and M. Rappaz: Solidification, EPFL Press, Lausanne, CH, (2009), 47, 177, 318.
13) G. H. Gulliver: *J. Inst. Met.*, **9** (1913), 120.
14) G. H. Gulliver: *J. Inst. Met.*, **11** (1914), 252.
15) G. H. Gulliver: *J. Inst. Met.*, **13** (1915), 263.
16) E. Scheil: *Z. Metallkd.*, **34** (1942), 70.
17) W. H. Press, B. P. Flannery, S. A. Teukolsky and W. T. Vetterling: Numerical Recipes: The Art of Scientific Computing, Cambridge University Press, Cambridge, UK, (1986), 359.
18) J. S. Langer and H. Muller-Krumbhaar: *J. Cryst. Growth*, **42** (1977), 11.
19) P. Shi: Public Ternary Alloy Solutions Database (2008), 1.3. Thermo-Calc software AB, Stockholm, SE.
20) S. Mosbah, M. Bellet and Ch.-A. Gandin: *Metall. Trans.*, **41A** (2010), 651.